

## The 19 Feb. 2016 Outburst of Comet 67P/CG: An ESA Rosetta Multi-Instrument Study

E. Grün,<sup>1,2\*</sup> J. Agarwal,<sup>3</sup> N. Altobelli,<sup>4</sup> K. Altwegg,<sup>5</sup> M. S. Bentley,<sup>6</sup> N. Biver,<sup>7</sup> V. Della Corte,<sup>8</sup> N. Edberg,<sup>9</sup> P. D. Feldman,<sup>10</sup> M. Galand,<sup>21</sup> B. Geiger,<sup>4</sup> C. Götz,<sup>36</sup> B. Grieger,<sup>4</sup> C. Güttler,<sup>3</sup> P. Henri,<sup>11</sup> M. Hofstadter,<sup>12</sup> M. Horanyi,<sup>2</sup> E. Jehin,<sup>13</sup> H. Krüger,<sup>3</sup> S. Lee,<sup>12</sup> T. Mannel,<sup>6</sup> E. Morales,<sup>46</sup> O. Mousis,<sup>32</sup> M. Müller,<sup>14</sup> C. Opitom,<sup>13</sup> A. Rotundi,<sup>8,15</sup> R. Schmied,<sup>6,16</sup> F. Schmidt,<sup>17</sup> H. Sierks,<sup>3</sup> C. Snodgrass,<sup>18</sup> R. H. Soja,<sup>17</sup> M. Sommer,<sup>17</sup> R. Srama,<sup>17</sup> C.-Y. Tzou,<sup>5</sup> J.-B. Vincent,<sup>3</sup> P. Yanamandra-Fisher,<sup>19</sup> M. F. A'Hearn,<sup>22</sup> A. I. Erikson,<sup>9</sup> C. Barbieri,<sup>23</sup> M. A. Barucci,<sup>7</sup> J.-L. Bertaux,<sup>24</sup> I. Bertini,<sup>25</sup> J. Burch,<sup>47</sup> L. Colangeli,<sup>20</sup> G. Cremonese,<sup>26</sup> V. Da Deppo,<sup>27</sup> B. Davidsson,<sup>28</sup> S. Debei,<sup>29</sup> M. De Cecco,<sup>30</sup> J. Deller,<sup>3</sup> L. M. Feaga,<sup>22</sup> M. Ferrari,<sup>8</sup> S. Fornasier,<sup>7</sup> M. Fulle,<sup>30</sup> A. Gicquel,<sup>3</sup> M. Gillon,<sup>13</sup> S.F. Green,<sup>18</sup> O. Groussin,<sup>32</sup> P. J. Gutiérrez,<sup>33</sup> M. Hofmann,<sup>3</sup> S. F. Hviid,<sup>34</sup> W.-H. Ip,<sup>35</sup> S. Ivanovski,<sup>8</sup> L. Jorda,<sup>32</sup> H. U. Keller,<sup>36</sup> M. M. Knight,<sup>22</sup> J. Knollenberg,<sup>34</sup> D. Koschny,<sup>20</sup> J.-R. Kramm,<sup>3</sup> E. Kührt,<sup>34</sup> M. Küppers,<sup>4</sup> P. L. Lamy,<sup>48</sup> L. M. Lara,<sup>33</sup> M. Lazzarin,<sup>23</sup> J. J. López-Moreno,<sup>37</sup> J. Manfroid,<sup>13</sup> E. Mazzotta Epifani,<sup>45</sup> F. Marzari,<sup>23</sup> G. Naletto,<sup>25,38</sup> N. Oklay,<sup>3</sup> P. Palumbo,<sup>8,15</sup> J. Wm. Parker,<sup>39</sup> H. Rickman,<sup>28,40</sup> R. Rodrigo,<sup>4,41</sup> J. Rodríguez,<sup>37</sup> E. Schindhelm,<sup>39</sup> X. Shi,<sup>3</sup> R. Sordini,<sup>8</sup> A. J. Steffl,<sup>39</sup> S. A. Stern,<sup>39</sup> N. Thomas,<sup>5</sup> C. Tubiana,<sup>3</sup> H. A. Weaver,<sup>42</sup> P. Weissman,<sup>43</sup> V. V. Zakharov,<sup>7,44</sup> and M. G. T. Taylor<sup>20</sup>

<sup>1</sup>Max-Planck Institut für Kernphysik, Saupfercheckweg 1, 69127 Heidelberg, Germany; <sup>2</sup>Laboratory for Atmospheric and Space Physics, University of Colorado, 1234 Innovation Dr, Boulder, CO, 80303, USA; <sup>3</sup>Max-Planck Institut für Sonnensystemforschung, Justus-von-Liebig-Weg, 3 37077 Goettingen, Germany; <sup>4</sup>European Space Agency (ESA), Camino Bajo del Castillo, s/n, 28692 Villanueva de la Canada, Madrid, Spain; <sup>5</sup>Physikalisches Institut, University of Bern, Sidlerstr. 5, CH-3012 Bern, Switzerland; <sup>6</sup>Space Research Institute, Austrian Academy of Sciences, Schmiedlstraße 6, 8042 Graz, Austria; <sup>7</sup>LESIA-Observatoire de Paris, CNRS, UPMC, Université Paris-Diderot, 5 place Jules Janssen, 92195 Meudon, France; <sup>8</sup>IAPS/INAF, Via del Fosso del Cavaliere, Roma, 00133, Italy; <sup>9</sup>Swedish Institute of Space Physics, Ångström Laboratory, Lägerhyddsvägen 1, Uppsala, Sweden; <sup>10</sup>Johns Hopkins University, Department of Physics and Astronomy, Baltimore, MD, USA; <sup>11</sup>LPC2E, CNRS, Orléans, France; <sup>12</sup>Jet Propulsion Laboratory/Caltech, 4800 Oak Grove Drive, Pasadena, CA 91109, USA; <sup>13</sup>Institut d'Astrophysique et de Géophysique, Université de Liège, Sart-Tilman, 4000 Liège, Belgium; <sup>14</sup>ESA/ESOC, Robert-Bosch-Str. 5, Darmstadt, Germany; <sup>15</sup>Dip. di Scienze e Tecnologia, Università degli Studi di Napoli Parthenope, CDN IC4, I-80143 Naples, Italy; <sup>16</sup>Institute of Physics, University of Graz, Universitätsplatz 3, 8010 Graz, Austria; <sup>17</sup>Institut für Raumfahrtssysteme (IRS), Universität Stuttgart, Pfaffenwaldring 29, 70569 Stuttgart, Germany; <sup>18</sup>Planetary and Space Sciences, Department of Physical Sciences, The Open University, Milton Keynes, MK7 6AA, UK; <sup>19</sup>Space Science Institute, 13456 Cajon Creek Court, Rancho Cucamonga CA 91739, USA; <sup>20</sup>European Space Research and Technology Centre, European Space Agency, Keplerlaan 1, NL 2201 AZ Noordwijk, The Netherlands; <sup>21</sup>Imperial College, South Kensington Campus, London SW7 2AZ, UK; <sup>22</sup>Department for Astronomy, University of Maryland, College Park, MD 20742-2421, USA; <sup>23</sup>Department of Physics and Astronomy "G. Galilei", University of Padova, Vic. Osservatorio 3, 35122 Padova, Italy; <sup>24</sup>LATMOS, CNRS/UVSQ/IPSL, 11 Boulevard d'Alembert, 78280 Guyancourt, France; <sup>25</sup>Centro di Ateneo di Studi ed Attività Speciali "Giuseppe Colombo" (CISAS), University of Padova, Via Venezia 15, 35131 Padova, Italy; <sup>26</sup>INAF Osservatorio Astronomico di Padova, Vicolo dell'Osservatorio 5, 35122 Padova, Italy; <sup>27</sup>CNR-IFN UOS Padova LUXOR, Via Trasea 7, 35131 Padova, Italy; <sup>28</sup>Department of Physics and Astronomy, Uppsala University, Box 516, 75120 Uppsala, Sweden; <sup>29</sup>Department of Industrial Engineering University of Padova Via Venezia, 1, 35131 Padova, Italy; <sup>30</sup>INAF-Osservatorio Astronomico, Via Tiepolo 11, I-34143 Trieste, Italy; <sup>31</sup>University of Trento, via Sommarive, 9, Trento, Italy; <sup>32</sup>Aix Marseille Université, CNRS, LAM (Laboratoire d'Astrophysique de Marseille) UMR 7326, 13388, Marseille, France; <sup>33</sup>Instituto de Astrofísica de Andalucía-CSIC, Glorieta de la Astronomía, 18008 Granada, Spain; <sup>34</sup>Institute of Planetary Research, DLR, Rutherfordstrasse 2, 12489 Berlin, Germany; <sup>35</sup>Institute for Space Science, National Central University, 32054 Chung-Li, Taiwan; <sup>36</sup>Institute for Geophysics and Extraterrestrial Physics, TU Braunschweig, 38106 Braunschweig, Germany; <sup>37</sup>Instituto de Astrofísica de Andalucía (CSIC), Glorieta de la Astronomía s/n, E-18008 Granada, Spain; <sup>38</sup>Department of Information Engineering, University of Padova, Via Gradenigo 6/B, 35131 Padova, Italy; <sup>39</sup>Southwest Research Institute, 1050 Walnut Street, Suite 300, Boulder, CO 80302, USA; <sup>40</sup>PAS Space Research Center, Bartycka 18A, 00716 Warszawa, Poland; <sup>41</sup>International Space Science Institute, Hallerstrasse 6, 3012 Bern, Switzerland; <sup>42</sup>Johns Hopkins University Applied Physics Laboratory, Laurel, MD; <sup>43</sup>Planetary Science Institute, 1700 East Fort Lowell, Suite 106, Tucson, AZ 85719, USA; <sup>44</sup>Sorbonne Universités, UPMC Univ Paris 06, CNRS, Laboratoire de Météorologie Dynamique, 4 place Jussieu, 75252, Paris, France; <sup>45</sup>INAF-OAR, Via Frascati 33, Monte Porzio Catone (Roma), 00078, Italy; <sup>46</sup>Jaicoa Observatory, Aguadilla, Puerto Rico, U.S.A.; <sup>47</sup>Southwest Research Institute, 6220 Culebra Rd., San Antonio, TX 78238, USA.; <sup>48</sup>Laboratoire d'Astrophysique de Marseille, UMR 7326 CNRS & Aix-Marseille Université, 38 rue Frédéric Joliot-Curie, 13388 Marseille cedex 13, France.

**ABSTRACT**

On 19 Feb. 2016 nine Rosetta instruments serendipitously observed an outburst of gas and dust from the nucleus of comet 67P/Churyumov-Gerasimenko. Among these instruments were cameras and spectrometers ranging from UV over visible to microwave wavelengths, in-situ gas, dust and plasma instruments, and one dust collector. At 9:40 a dust cloud developed at the edge of an image in the shadowed region of the nucleus. Over the next two hours the instruments recorded a signature of the outburst that significantly exceeded the background. The enhancement ranged from 50% of the neutral gas density at Rosetta to factors  $>100$  of the brightness of the coma near the nucleus. Dust related phenomena (dust counts or brightness due to illuminated dust) showed the strongest enhancements (factors  $>10$ ). However, even the electron density at Rosetta increased by a factor 3 and consequently the spacecraft potential changed from  $\sim -16$  V to  $-20$  V during the outburst. A clear sequence of events was observed at the distance of Rosetta (34 km from the nucleus): within 15 minutes the Star Tracker camera detected fast particles ( $\sim 25$  m s $^{-1}$ ) while 100  $\mu$ m radius particles were detected by the GIADA dust instrument  $\sim 1$  hour later at a speed of 6 m s $^{-1}$ . The slowest were individual mm to cm sized grains observed by the OSIRIS cameras. Although the outburst originated just outside the FOV of the instruments, the source region and the magnitude of the outburst could be determined.

**Key words:** comets: individual: 67P/Churyumov-Gerasimenko – comets: general –

**1 INTRODUCTION**

In August 2014 the Rosetta spacecraft arrived at comet 67P/Churyumov-Gerasimenko (67P). Since then, the spacecraft has been accompanying the comet on its journey around the Sun (Glassmeier et al. 2007). During that time Rosetta used all its instruments to closely study the nucleus and its activity. In August 2015 Rosetta and 67P passed through perihelion at a distance of 1.25 AU from the sun, and a firework display of cometary outbursts was observed Vincent et al. (2016). Six months later on 19 Feb. 2016 nine Rosetta instruments serendipitously observed an outburst of gas and dust from the nucleus of 67P. This paper is the first report of this most extensively studied cometary outburst.

The observations were carried out during the Rosetta mission extended phase, very close to the end of the intensive summer that the southern hemisphere of the comet experienced between May 2015 and March 2016. A large number of observations were under way in order to obtain final measurements to characterise the Southern hemisphere before it re-entered polar night, and to observe the return of the northern hemisphere from its shorter polar night. Ground based observations were most favourable during early 2016 because the comet was still relatively active (as exemplified by the event discussed in this paper) and was visible in the night sky as observed from Earth. During 2015 the spacecraft had been flying at greater distances from the comet than originally foreseen, in order to avoid the navigational interference caused by the appearance of dust particles in the star tracker cameras. Therefore, at perihelion the spacecraft was at a distance of around 400 km from the comet, as a result of the high dust fluxes produced at this time. The period discussed in this paper was particularly focused on achieving the lowest possible altitudes by orbiting in the terminator plane. As such, it was the first time the spacecraft had been within 50 km of the comet since April 2015. These lower altitudes were designed to examine surface changes

due to perihelion passage and the seasonal effects of the approach of equinox. In addition, an overall target for the mission had been to investigate ‘active’ areas and ‘jets’ from their origin at the surface of the comet to in-situ at the spacecraft. However, such observations had been difficult to target specifically. Such a serendipitous event with the instrument coverage of 19 February 2016 was therefore most welcome. Earlier plans to perform an Activity Campaign by flying through a dust jet with all instruments monitoring the gas and dust environment and the source region on the nucleus underneath had been abandoned because of the star tracker interferences.

By 19 February 2016 the heliocentric distance had increased to almost twice the perihelion distance to 2.4 AU. Rosetta flew hyperbolic arcs between 42 and 32 km with a speed relative to the comet centre of 0.174 m s $^{-1}$  (Fig. 1). At 10:00 on 19 Feb. the distance of Rosetta from the centre of the comet was 34.5 km, the angular size of the nucleus was about 8°, and the solar phase angle was 63°. Rosetta was above the southern hemisphere of 67P on the morning side at local time 07:51:37 (referring to the illumination by the sun). The sub-S/C latitude was  $-30^\circ$  and the longitude was  $301^\circ$  in the Cheops Reference Frame.

Science operations on 19 Feb. called for (1) dust monitoring by the OSIRIS imaging system followed by (2) a global coma scan by the microwave instrument MIRO with the Alice UV spectrograph and OSIRIS co-riding. OSIRIS dust monitoring required off-limb pointing for the Narrow Angle Camera NAC and the Wide-Angle Camera WAC (Fig. 1), covering in duration at least a full nucleus rotation of about 12 hours. The fourth remote-sensing instrument VIRTIS, an infrared imaging spectrometer, was monitoring the illuminated nucleus whenever allowed by the dust-monitoring pointings of OSIRIS and MIRO. All in-situ instruments monitored, in parallel, dust (GIADA), gas (ROSINA), and plasma (RPC). In addition the dust collectors of MIDAS were exposed to the environment all day. Science observation periods of about 4 hours were interrupted by Nadir pointing navigation and maintenance

\* E-mail: eberhard.gruen@mpi-hd.mpg.de

activities of about 1 hr and 0.5 hr duration, respectively. The latter technical activities involved observations by the Star Tracker (STR) and the Navigation Camera (NAVCAM). The OSIRIS dust monitoring campaign staring just above the sub-solar limb ( $\sim 4^\circ$  from Nadir, Fig. 2) started 18 February UT 21:52:51 and ended on the next day at 12:42:09. The following global coma scan by MR required pointing of up to  $70^\circ$  away from Nadir.

About 2 days after the data were taken they were transmitted to the ground and accessible by the instrument teams. In the morning of 22 February the GIADA team reported a large flux of compact dust particles between 10:00 and 13:00 on 19 February. The operations team responded that the STR saw a huge increase in background noise in the same time period. The ROSINA team reported a correlated peak in the neutral gas density. Observers on the ground suggested from preliminary photometry of 67P with the Transiting Planets and Planetesimals Small Telescope (TRAPPIST) at ESO's La Silla Observatory an increase in total brightness. A search of the NAVCAM images resulted in images that showed local dust coma brightness enhancements near the nucleus. In addition the Langmuir probes of the Rosetta Plasma Consortium (RPC-LAP) found the spacecraft potential to drop from about -15 to -20 V by about 10:00 on 19 Feb. and then slowly go back during the hours after. In the following days MIRO also reported changes in the coma temperature in the same time period. MIDAS also collected plenty of dust during the collection period that included 19 February. The break-through in understanding of what had happened came about three weeks later when the OSIRIS team presented WAC and NAC images that showed the history of the outburst on 19 February and indicated the potential source region.

In Section 2 we give a detailed description of the observations by various instruments, including some ground-based observations. In Section 3 the timing of the different observations is compared in order to pin-down the exact time of the outburst and identify the potential source region and the magnitude of the outburst. A summary of the results and a comparison with previous outbursts during the perihelion passage is given in Section 4 including a discussion of further studies and potential mechanisms.

## 2 OBSERVATIONS

Details of the positive observations of the outburst from Rosetta and ground based astronomical observations are discussed in the following sections. Their order reflects the approximate time order of the maximum signals recorded. First were the OSIRIS and NAVCAM series of camera images and the ALICE UV observations, followed by the MIRO microwave observations, the RPC plasma and the ROSINA COPS gas density measurements. Later came the Star Tracker brightness measurements, and the GIADA dust detections and the MIDAS dust collections. These Rosetta observations are complemented by ground-based observations of coma and tail.

No relevant observations were made by VIRTIS because the VIRTIS-Mapper was looking at the sub solar limb, with the slit located away from the source region. No dust was collected by the COSIMA dust mass analyser during 19 Febru-

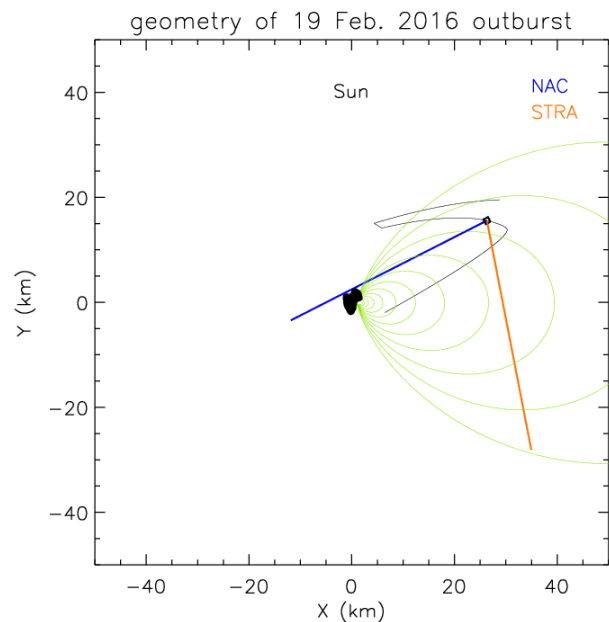


**Figure 1.** Observation geometry (right) in Sun-67P-Rosetta plane on 19 Feb. 10:00. Black line: projection of trajectory from 15 to 24 Feb. 2016; Square: Rosetta position; blue line: line-of-sight (LOS) of remote sensing instruments (OSIRIS NAC and WAC, Alice, NAVCAM); red line: projection of LOS of Star Tracker A (STR-A); green: schematic evolution of a dust plume.

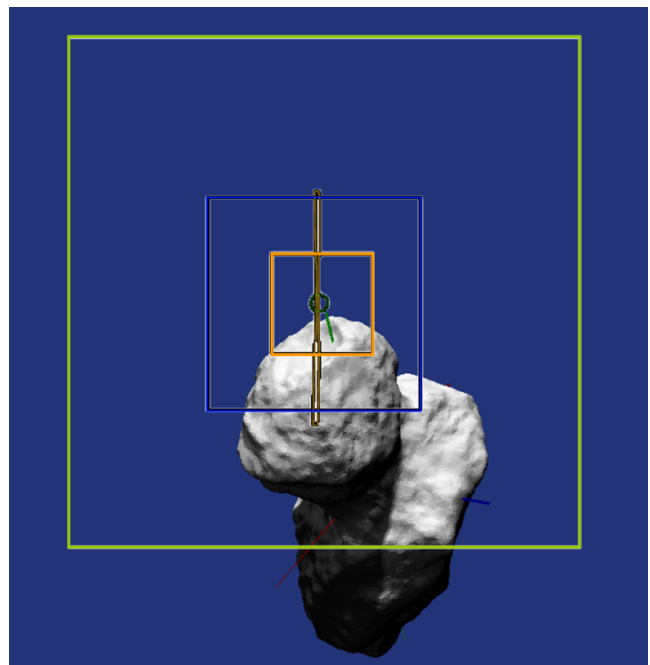


**Figure 2.** Model image (generated by the CG Model viewer <https://planetgate.mps.mpg.de:8114/>) showing the nucleus and its illumination at 9:40 in the perspective from Rosetta. The Sun is up. The squares of decreasing size are the fields of view (FOVs) of the WAC, NAVCAM, and NAC cameras, respectively. The vertical bar represents the Alice slit and the small circle is the MIRO sub-millimetre beam. The short red, dark green, and blue bars indicate the principle axes of the nucleus.

ary because it was in the dust analysing mode during that period. The Radio Science Investigation (RSI) did not see a sign of the outburst in the radio signal from Rosetta. Also measurements of the gas drag from momentum wheel measurements by the attitude and articulation system of the spacecraft were unfavourable during the outburst time period.

## 2.1 OSIRIS

The Optical, Spectroscopic, and Infrared Remote Imaging System (OSIRIS, Keller et al. (2007)) on board the Rosetta spacecraft consists of a Narrow- and a Wide Angle Camera (NAC) and (WAC), each having a  $2048 \times 2048$  pixel CCD detector, and fields of view (FOVs) of approximately  $2^\circ \times 2^\circ$  and  $12^\circ \times 12^\circ$ , respectively. The cameras have regularly imaged the nucleus and coma of 67P since March 2014 in 25 broad- and narrow-band filters covering the wavelength range 240 to 1000 nm (Sierks et al. 2015). The standard data processing on ground comprises bias-subtraction, flat-fielding, correction for distortion of the optical path, and flux calibration relative to standard stars.

From 18 Feb. 21:56 to 19 Feb. 12:10, OSIRIS obtained 1 NAC and 2 WAC images approximately every 30 minutes. The NAC images were taken in the orange filter (centred at 649 nm with a bandwidth of 85 nm, exposure time 3.75 s), and the WAC images were obtained using the green (537 nm, 63 nm, 3 s) and red (630 nm, 157 nm, 1.5 s) filters. At the 34.5 km distance of the comet from the spacecraft, the FOVs covered 1.4 km (NAC) and 6.9 km (WAC). The instrument boresights were pointed at the subsolar limb. The WAC images cover a significant part of the nucleus.

As shown by Fig. 3, up until 19 Feb 9:10 the images show a typical coma composed of faint dust structures. The nucleus has deep shadows and illuminated surfaces that are saturated on the detector, because the exposure times were optimized to capture the faint dust coma. The WAC images obtained at 9:40, however, show a brightening strong enough to saturate the detector in a region where the nucleus should be in shadow. By 10:10, the bright cloud had expanded across the entire WAC FOV, saturating the detector in front of the whole visible part of the big nucleus lobe. At 10:40 the overall coma brightness had diffused, but a large part of the shadowed nucleus was still hidden behind bright foreground dust. The dust diffused slowly in the following images, and several narrow coma structures became visible. These could be related to the outburst, but some may also reflect the typical activity of this region and local time.

The coma surface brightness as a function of time was measured in two reference areas in the FOVs of NAC (above the sun-lit limb) and WAC (in the lower left corner of the image). These were chosen to be sufficiently distant from the saturated area and from the limb, in order to minimize rotation-induced changes of the brightness as a consequence of changing limb-distance from the irregularly shaped nucleus. In the WAC reference area, located near the source region, the surface brightness of the coma (corresponding to the total dust cross-section) increased by two orders of magnitude between 9:40 and 10:10, and decreased back to a factor 10 above the pre-outburst level in the last image obtained at 12:10 (Fig. 4).

The NAC images were zoomed and stretched to such detail that individual grains became visible. After subtracting the local background the image sequence shows a transition from a point-like granularity (grains that were distant or slow enough to appear as points) to a more linear texture dominated by grains either close or fast enough to be trailed across several pixels. The transition occurred between 11:10 and 11:40.

In the afternoon of 19 February, from 14:30 to 21:30, OSIRIS took NAC and WAC images during a MIRO Great Circle Scan pointing most of the time far from nadir. At 14:30, the coma surface brightness was still one order of magnitude higher than at reference epochs with similar pointing. It decreased to normal level at 21:30, i.e. about one spin period after the start of the outburst.

## 2.2 NAVCAM

The Navigation Camera (NAVCAM) is part of the spacecraft sub-systems. It is used by the Flight Dynamics team in order to determine the relative position between Rosetta and the comet nucleus. Its images are therefore essential for safely navigating the spacecraft in the comet environment. In addition, context images for scientific observations are also scheduled on request of the instrument teams.

There are two identical NAVCAMs on board the spacecraft, although only one of them is used in nominal operations. The camera's field of view is  $5^\circ \times 5^\circ$  and its CCD detector consists of  $1024 \times 1024$  pixels. The spectral sensitivity covers the visible wavelength range from approximately 550 to 850 nm. A mechanism makes it possible to select between different optical elements with or without attenuation coating. There are no spectral filters.

During the period of the outburst event NAVCAM context images without attenuation were acquired at 08:21, 10:14, and 12:29. Afterwards a navigation raster comprising four images at 12:51, 12:55, 13:01, and 13:05 was carried out with the attenuation filter. The uncalibrated data are available in the ESA Planetary Science Archive (Geiger and Barthelemy 2016).

A preliminary version of the foreseen radiometric calibration procedure Geiger et al. (2016) was applied in order to transform the raw pixel values to average spectral radiance values in the broad visible wavelength range. Fig. 5 depicts the two images acquired at 12:29 and 12:55. The NAVCAM images show that the collimated dust emission seen in the last images of the OSIRIS sequence (cf. Fig. 3) continues as the nucleus rotates. In addition to the diffuse component a few individual objects can be seen in the coma. However, from the images it is not possible to determine the distance from the spacecraft and hence the size of these objects.

## 2.3 Alice

Alice is a far-ultraviolet (70 to 205 nm) imaging spectrograph on board Rosetta that, amongst multiple objectives, is designed to observe emissions from various atomic and molecular species from within the coma of comet 67P (Feldman et al. 2015) as well as reflected solar radiation from both the nucleus and the dust coma (Stern et al. 2015;

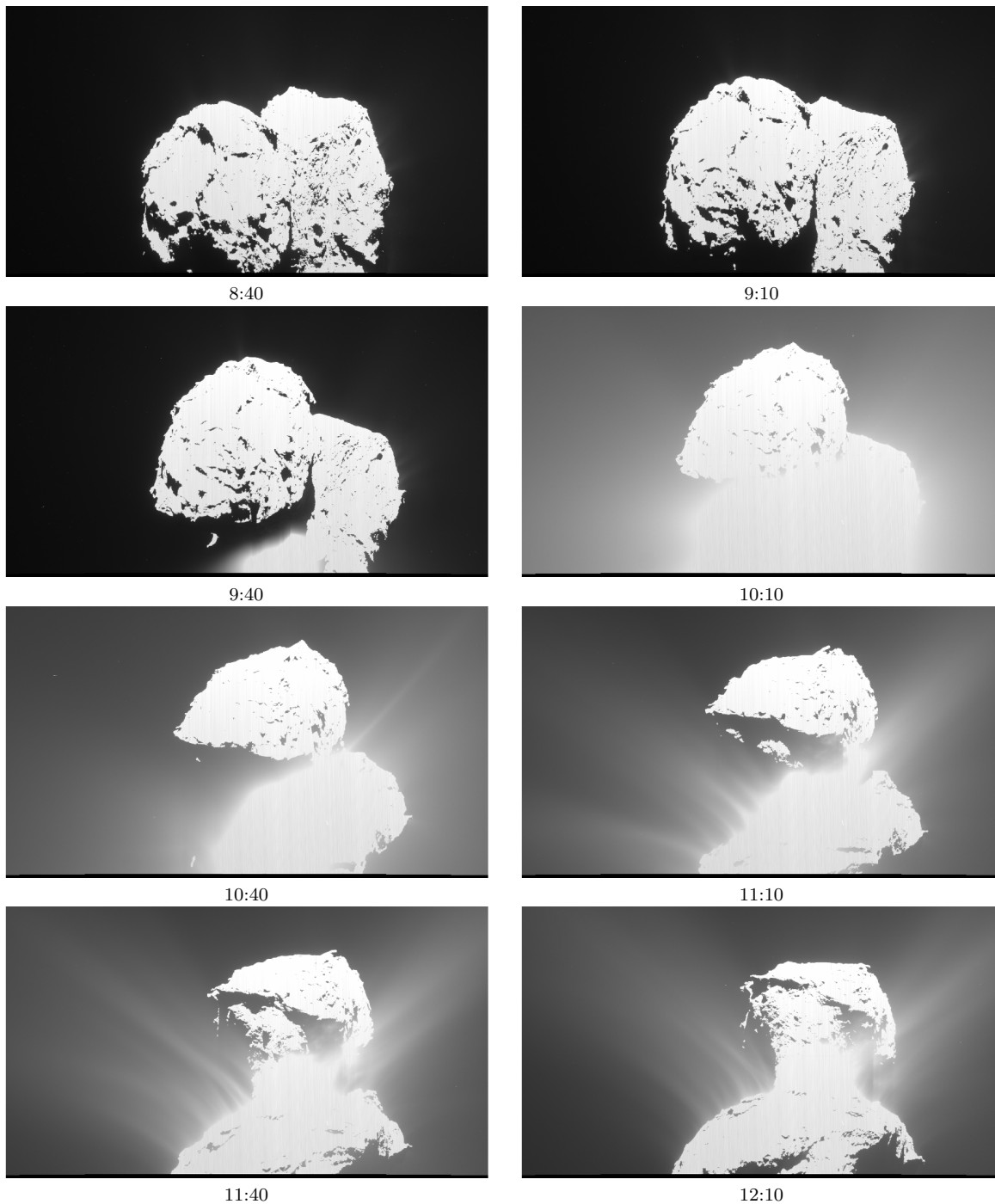


**Figure 3.** OSIRIS WAC images taken at 8:40, 9:10, 9:40, 10:10, 10:40, 11:10, 11:40, and 12:10, respectively. Each image is about  $11.5^\circ \times 6.2^\circ$  in size, they were obtained in the broadband green filter with 3 second exposure time. The image brightness is scaled according to the square root of the measured flux, with minimum and maximum values of  $1.5 \times 10^{-7}$  (black) and  $1.5 \times 10^{-4} \text{ W m}^{-2} \text{ sr}^{-1} \text{ nm}^{-1}$  (white). The Sun is at the top.

Feaga et al. 2015). The spectrograph slit is in the shape of a dog bone,  $5.5^\circ$  long, with a width of  $0.05^\circ$  in the central  $2.0^\circ$ , while the ends are  $0.10^\circ$  wide, giving a spectral resolution between 0.8 and 1.2 nm for extended sources that fill its field-of-view. Each spatial pixel or row along the slit is  $0.30^\circ$  long. Details of the instrument have been given by Stern et al. (2007).

In particular, Alice is able to address the timing and du-

ration of the event. The Alice observations were made with the small lobe of the nucleus in the lower half of the slit and the coma above the sunward limb in the upper half, as shown in Fig. 2. A spectrum taken on 19 Feb. 11:19:44 is shown in Fig. 6. A light curve derived from the Alice spectra is shown in Fig. 7. In two successive 10-minute histograms beginning at UT 09:45:59 Alice observed a  $\sim 50\%$  increase in brightness in the direction of the small lobe of the nucleus. Considering

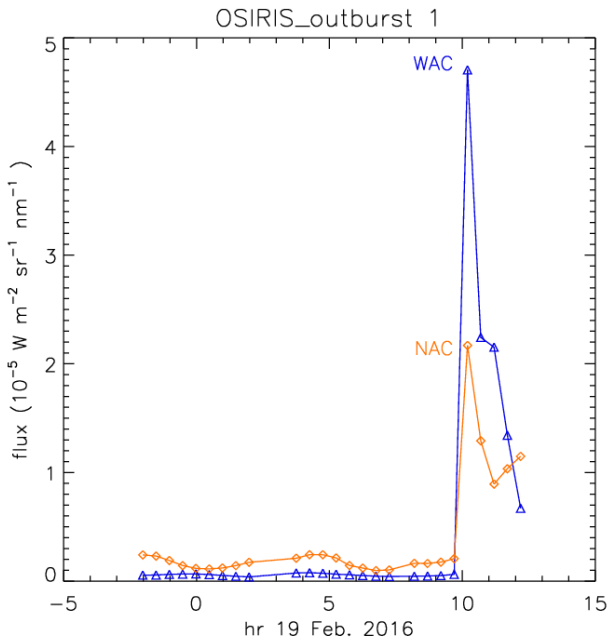


**Figure 4.** Surface brightnesses measured in the WAC and NAC reference areas.

the 10-minute integration time of the Alice data, the onset time is consistent with that reported by the other remote sensing instruments on Rosetta. At the same time the dust coma brightness increased by a factor of  $\sim 5$  and remained at that level for  $\sim 30$  minutes. The following histograms had contamination of the coma from a bright star in the field-of-view leading to a 20-minute data gap. From UT 11:10 until the end of the observation sequence at  $\sim 12:30$  the coma brightness remained at a value of  $\sim 2.5$  times the prior quiescent level. There were no further Alice observations with the same viewing geometry on 19 February. The same data do not show any significant gas emissions at the time of the outburst.

## 2.4 MIRO

MIRO (Microwave Instrument for the Rosetta Orbiter) is a small radio telescope working at millimetre and submillimetre wavelengths (Gulkis et al. 2007). It has broadband continuum receivers designed to measure the sub-surface properties of the nucleus and to study dust in the coma. MIRO also has a high-resolution spectrometer, which can be used to probe the abundance, temperature, and velocity of several coma gases, including  $\text{H}_2\text{O}$ . MIRO is calibrated against two internal targets approximately every 30 minutes, and can also be calibrated against dark sky measurements when looking far from the nucleus. Here we focus on some of MIRO's spectral observations during the outburst. A more complete description of MIRO's view of the outburst is in Hofstadter et al. (2016).

MIRO is a single-pixel instrument. From about 08:10 to 12:30 on 19 February 2016 Rosetta was performing a stare above the sub-solar limb (Fig. 2). Most of that time MIRO's footprint was above the limb, but from about 09:30 to 11:00

the rotation of the nucleus brought parts of the surface into its line-of-sight.

Water vapour all along MIRO's line-of-sight contributes to the received signal, so interpreting the spectrum at all frequencies requires detailed consideration of the three-dimensional structure of the coma. Given the strength of the water line, however, there are frequencies at which the coma is optically thick, and MIRO senses only the gas relatively close to the spacecraft. The received signal is remarkably constant at these frequencies. Even as the nucleus moves into and out of MIRO's LOS, the signal does not change because the nearby gas screens the view of everything beyond it. Under these optically thick conditions, the amount of radio energy received is set by the rotational temperature of the gas.

Figure 8 shows the radio emission from the coma at an optically thick frequency, expressed as a brightness temperature. The frequency chosen corresponds to the  $\text{H}_2^{16}\text{O}$  line center for gas moving at 620 m/s toward the spacecraft. The  $\text{H}_2^{16}\text{O}$  spectrum in this region shows features indicative of being optically thick (Hofstadter et al. (2016)) and the  $\text{H}_2^{18}\text{O}$  line shape confirms the gas expansion velocity is near 600 m/s. In the figure, the brightness temperature rise of the gas by about 30 K was starting just before 10:00 on 19 February, followed by a slow decrease for several hours. At about 12:30 the spacecraft began pointing to different areas of the coma, and the measurements can no longer be directly compared to those shown. It is interesting to note that one nucleus rotation (about 12.4 hours) before the outburst, the nucleus orientation and MIRO's observing geometry were similar to that during the outburst. Figure 8 also shows that the temperature of the coma at that time (times from -2:00 to 00:00) is consistent with the values measured just before the outburst. This demonstrates that the change occurring near 10:00 is not due to normal diurnal variations.

Hofstadter et al. (2016) explore three possible explanations for the increase in coma temperature. One is that the gas during the outburst is coming from a source region on the nucleus with a significantly higher physical temperature than the normally sublimating regions. Another possibility is that the local gas density during the outburst, either above or below the surface, increased enough to alter the adiabatic cooling expected as the gas expands into a near vacuum. The third explanation we are exploring is that the gas is warmed by the dust either via collisions or radiation. Gas by itself cools adiabatically very quickly as it expands into space, whereas dust by itself can stay warm because it cools radiatively much more slowly.

An important clue, discussed later (see Fig. 18 below), is that the increase in gas temperature near the spacecraft observed by MIRO occurs several minutes after dust is first seen rising from the nucleus, but several minutes before the local gas density increases. Note that dust travelling at metres per second takes over an hour to travel from the nucleus to the spacecraft, while gas moving at  $620 \text{ m s}^{-1}$  takes only about a minute. The relative timing of rising dust at the surface, the increase in gas temperature at the spacecraft, and then the increase in gas density at the spacecraft, is not yet understood.

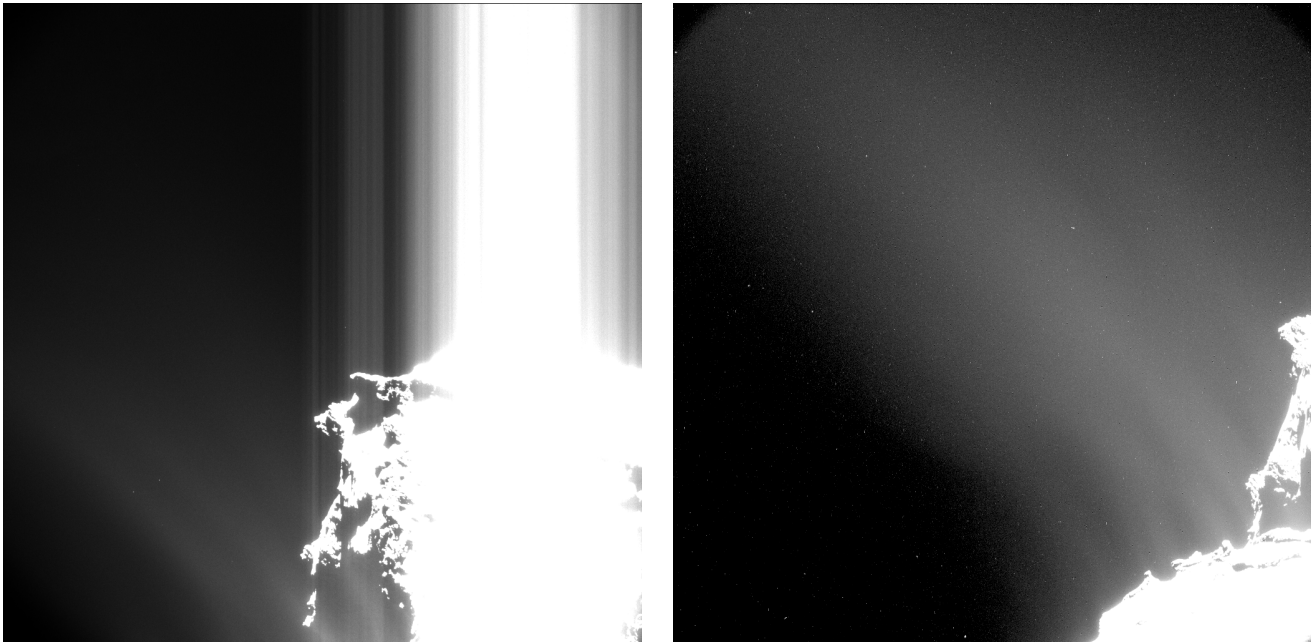


**Figure 5.** NAVCAM images acquired at 12:29 (left) and 12:55 (right). The first image was taken without attenuation filter and 0.01 sec exposure time. The vertical structures towards the top right are blooming artefacts due to saturation on parts of the nucleus. The second image is part of a navigation raster with attenuation filter and 1.75 sec exposure time. The grey scales were adapted such that the maximum (white colour) corresponds to  $1 \times 10^{-4} \text{ W m}^{-2} \text{ sr}^{-1} \text{ nm}^{-1}$ .

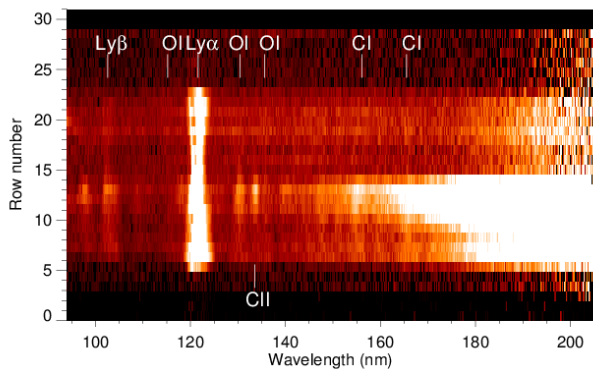


**Figure 6.** An Alice spectral image beginning at UTC 11:19:44 showing the solar reflected radiation from the nucleus in the lower right. Dust in the coma shows up in the upper right. The orientation of the slit is as shown in Figure 2. The integration time was 1814 s.

## 2.5 RPC

The Rosetta Plasma Consortium (RPC, Carr et al. (2007)) is a suit of five plasma sensors to monitor the electromagnetic field and the ionised environment around 67P. Among the RPC sensors, RPC-MIP (Mutual Impedance Probe, Trotignon et al. (2007)) and RPC-LAP (Langmuir Probes, Eriksson et al. (2007)) measure the plasma density. Following the increase in neutral density by a factor of about 1.8 (ROSINA-COPS, section 2.6), MIP and LAP observed a local plasma density increase by a factor of about 2.7 to 3 during the outburst, both through the electron plasma frequency increase (MIP) and (negative) spacecraft potential increase (LAP), as shown in Figs. 9 and 10. The spacecraft

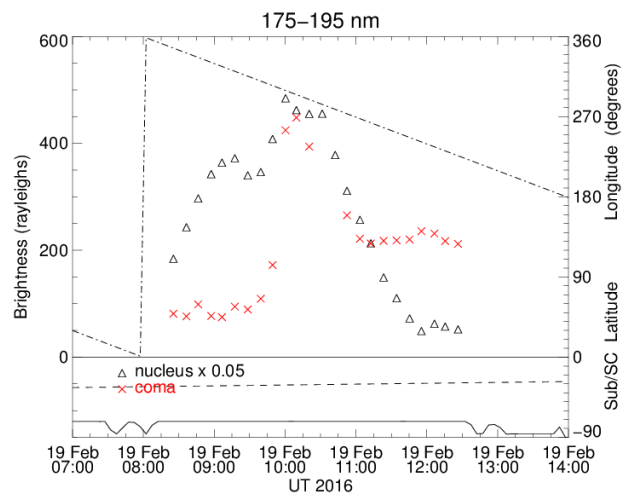


**Figure 7.** Light curve of the reflected solar radiation (175–195 nm) seen by Alice. The times represent the mid-points of each 10-minute integration. The enhancement in emission seen towards the nucleus is superimposed on a smooth variation due to changes in geometry as the comet rotates. The sub-spacecraft longitude (dot-dashed line) and latitude (dashed line) are also shown. The line near the bottom shows the  $3^{\circ}58'$  offset of the boresight from nadir towards the Sun.

potential is proportional to the logarithm of the electron density. Note that a local decrease in the plasma density is observed just before the onset of the outburst, around 9:45 UT. The energetic electrons observed during the outburst are colder than before and after the outburst, as suggested by RPC-IES electron spectra (Ion and Electron Spectrometer, Burch et al. (2007)). This would be consis-

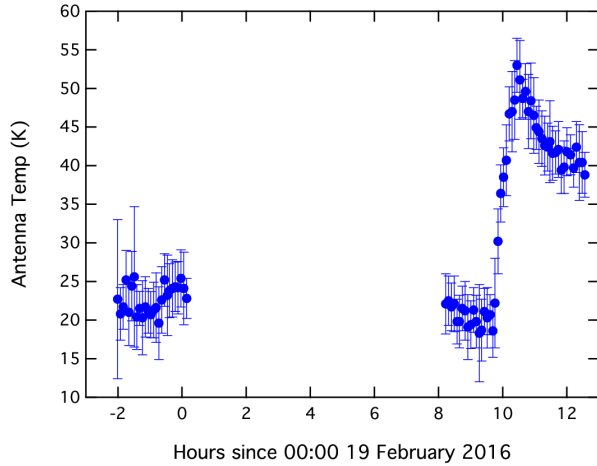


**Figure 8.** Time evolution of the  $\text{H}_2\text{O}$  excitational temperature of the gas near the spacecraft, as measured by gas moving at a velocity of  $620 \text{ m s}^{-1}$  towards the observer (see text). MIRO collected spectral data every 30 seconds. The indicated points represent a 5-minute average of those data, with error bars being the rms deviation of the 10 spectra in each average.

tent with electron cooling during the outburst, in the region between the comet and the spacecraft. Such cooling may be the signature of an increase in electron-neutral collisions, which is consistent with the observed increase in the neutral density (section 2.7). Those collisions may have increased the local ionisation by electron impact in the region between the comet and the spacecraft. An increase in the ionisation source closer to the comet could explain the significant relative increase in plasma density, which is larger than the relative increase in neutral density, observed at Rosetta during the outburst. However, other possible explanations exist, such as a reduced neutral outflow velocity or changes in composition. Further studies are needed to identify the exact mechanisms causing the variable plasma density as well as the faster plasma density decay compared to the neutral density decay. Finally, the plasma density relaxes to the pre-outburst value around 12:00 UT, faster than the neutral density, while cold electrons are still observed until 14:00 UT.

While the electron density increased, the average magnetic field measured by RPC-MAG (Magnetometer, Glassmeier et al. (2007a)) increased slightly from 16 nT to 19 nT. This change was mostly in the y-direction, meaning the direction in the ecliptic that is perpendicular to the Sun-comet line. At the same time the power spectral density in the range of 50-100 mHz decreased by about a factor 1/2.

## 2.6 ROSINA

ROSINA is designed for in-situ measurements of the cometary coma gas density and composition (Balsiger et al. 2007). The instrument package consists of two complementary mass spectrometers (DFMS and RTOF) for neutrals and primary ions and a pressure sensor (COPS). ROSINA-COPS is an in-situ instrument consisting of two separate sensors, described by Balsiger et al. (2007). The nude gauge (NG) measures the total ambient neutral gas number density at the spacecraft position and the ram gauge, which is

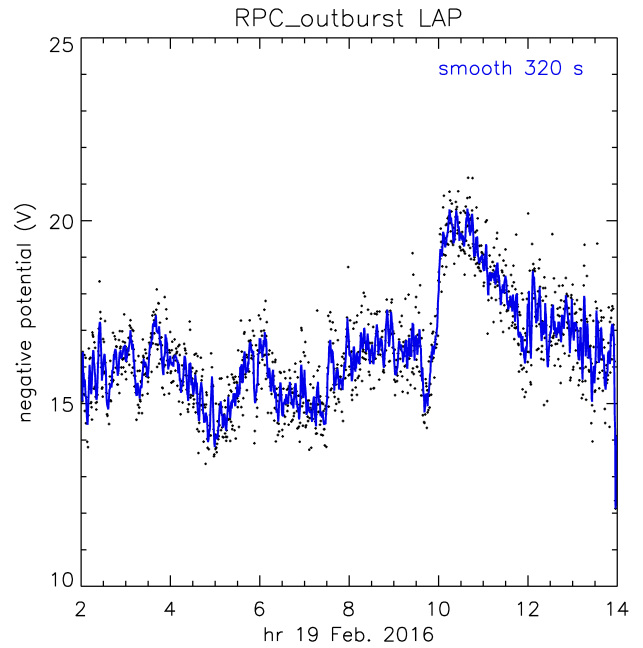


**Figure 9.** The negative spacecraft potential as determined by RPC-LAP. Individual measurements (dots) and smoothed signal (blue line).

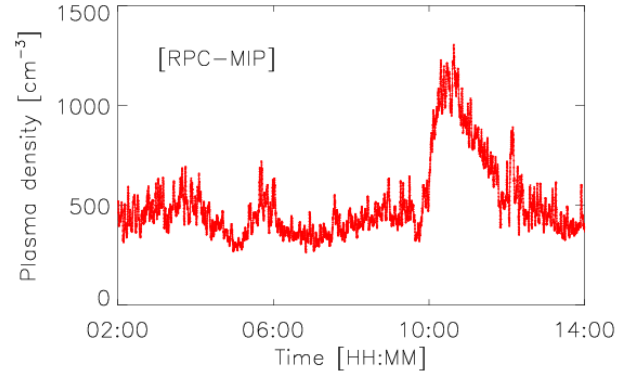


**Figure 10.** Plasma density measured by RPC-MIP.

normally pointing at the comet, measures the ram pressure of the outflowing gas of coma. All data presented in this study are from the NG sensor only. The neutral gas density is determined from the sensor signal as a linear combination of the abundances of the dominant species  $\text{H}_2\text{O}$ ,  $\text{CO}_2$ ,  $\text{CO}$ , and  $\text{O}_2$  which are obtained by DFMS spectrometer measurements (Hässig et al. 2015).

The neutral gas density is modulated by the spacecraft location around the nucleus and the nucleus illumination conditions. Because of the highly irregular shape of the nucleus, the gas production varies by about a factor of 2 depending on the face that is illuminated by the Sun (Bieler et al. 2015). On 19 Feb. the neutral gas density (Fig. 11) showed fluctuations of up to  $10^8 \text{ cm}^{-3}$  due to the nucleus rotation. However, at  $\sim 10:00$  the gas density rapidly increased to almost  $1.5 \times 10^8 \text{ cm}^{-3}$  which is more than 50%

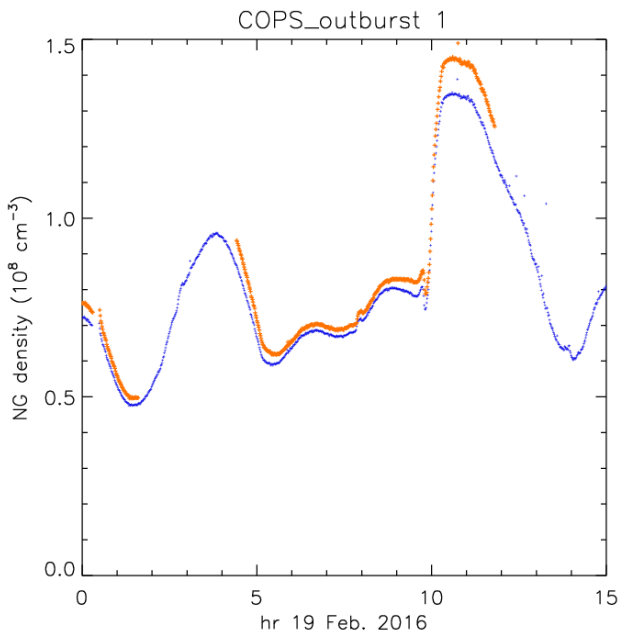


**Figure 11.** Neutral gas density (red) and uncalibrated COPS signal (blue, arbitrary units) during 19 Feb. 2016. Calibration was only applied when DFMS measurements were available. During MR global coma scan starting at 13:00 the coma gas was contaminated by spacecraft outgassing.

higher than the normal fluctuations at a similar nucleus phase.

## 2.7 Star Tracker

The autonomous attitude control system of the spacecraft relies on Star Tracker measurements as the main source of information (Buemi, Landi, & Procopio 2000). The field of view of the Star Tracker camera has a size of  $16.4^\circ \times 16.4^\circ$ . The characteristics of its CCD detector are identical to those of the NAVCAM, i.e.  $1024 \times 1024$  pixels and a broad spectral sensitivity in the visible wavelength range.

For redundancy two identical Star Trackers are available (STR-A and STR-B). Although they are both mounted on the -X-face of the spacecraft, their boresight directions differ by  $\approx 30^\circ$ . In the period of interest STR-A was continuously active in the closed attitude control loop. In addition, STR-B was switched on for 15 minutes at around 13:00 UTC for a regular attitude acquisition test.

In their operational modes the Star Trackers track the positions and magnitudes of up to 9 stars in the field of view. Housekeeping telemetry downlinked to ground includes a parameter that reports the mean background signal in  $20 \times 20$  pixel windows centred on the tracked stars. The value of this parameter quantifies the diffuse light contribution due to scattering by unresolved dust particles and provides valuable information about the temporal evolution of the outburst event.

We converted this parameter value into spectral radiance units by subtracting a bias value estimated from the available time series during the whole mission and by applying a calibration coefficient determined from the magnitude

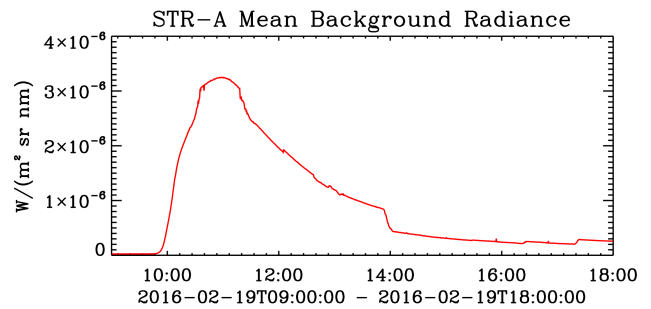


**Figure 12.** Temporal evolution of the mean background radiance measured by Star Tracker A (STR-A) during the outburst event. The results are derived from a housekeeping telemetry parameter which reports the mean background signal in  $20 \times 20$  pixel windows around the (up to 9) tracked stars.

conversion relations specified by the manufacturer in the on-board software. The uncertainty of this rough radiance calibration is expected to be in the order of 50% or better. The spectral radiance values should be understood as a weighted average over the broad visible sensitivity range.

The temporal evolution of the STR-A mean background radiance on 19 February is shown in Fig. 12. At the beginning of the depicted period the signal is at the noise level. However, shortly before 10:00 UTC the measured background radiance sharply increases, reaches its maximum at 11:00 UTC, and then slowly decreases. The step at about 14:00 UTC is due to a significant attitude change of the spacecraft due to the MIRO global coma scan. Before that time the spacecraft +Z-axis pointed towards the nucleus and consequently the STR-A boresight pointed  $90^\circ$  off-nucleus.

The radiance values measured by STR-B during its short operating period are in the same order as the STR-A results. Their quantitative difference is consistent with the different boresight directions of the two Star Trackers.

## 2.8 GIADA

GIADA (Grain Impact Analyzer and Dust Accumulator) consists of three subsystems: 1) the Grain Detection System (GDS), which detects dust particles as they pass through a laser curtain and provides particle speeds and their optical cross section; 2) the Impact Sensor (IS) measures particle's momentum from their impact on a plate connected to five piezoelectric sensors, which combined with the GDS detection time provides the particle speed and mass; 3) the Micro Balances System (MBS) provides the cumulative dust flux of grains smaller than  $10 \mu\text{m}$  (Della Corte et al. 2014), by using five quartz crystal microbalances in roughly orthogonal directions. Calibration activity performed on GIADA by means of cometary analogues (Ferrari et al. 2014) mean that it is possible to convert the GDS signal to the dust particle geometrical cross section (Della Corte et al. 2016), and thus to constrain the particle density (Rotundi et al. 2015). GIADA disentangled two particle families (Della Corte et al. 2015) present in the 67P coma: high density aggregates (detected by GDS and IS together and by IS alone), i.e. compact particles, and low density porous aggregates (detected by GDS alone), i.e. fluffy particles. GIADA observed an exceptional dust detection rate on the 19th of February 2016: 188

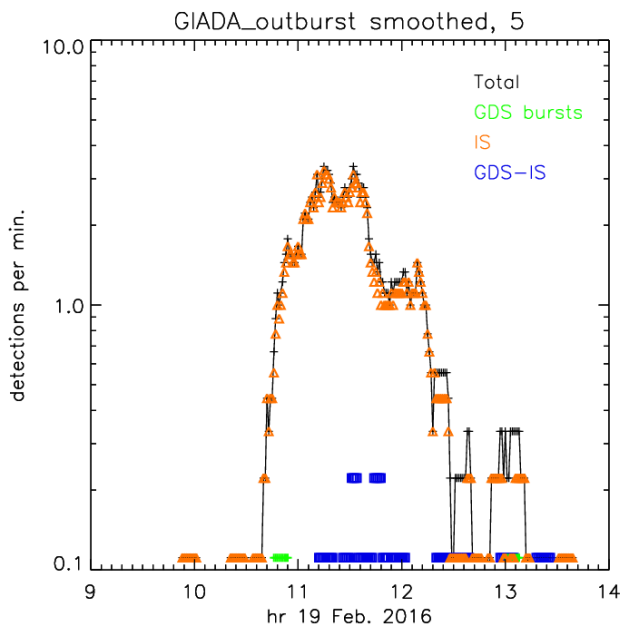


**Figure 13.** Rate of GIADA dust detections (total: black) and by its subsystems GDS-IS (blue), IS (red), and GDS bursts (green). The individual counts were smoothed with a 9-minute running average.

compact particles detected from 10:25:41 to 13:35:47 (Fig. 13) and 5 dust showers (Fulle et al. 2015) representing a total of 386 fluffy particles, 359 of which were detected from 17:27:35 to 17:28:00. The 5 dust showers are counted in the following only as 5 individual events since Fulle et al. (2015) suggest that the showers are caused by electro-static break-up of very fluffy agglomerates of sub-micron grains close to the Rosetta spacecraft. This is compared to a mean detection rate of  $\sim 3$  compact particles/day for most of the month of February 2016. For the GDS-IS detections GIADA provides directly particle speed, mass, and density. However, some assumptions have to be made in order to acquire the same information from detections on IS alone Della Corte et al. (2016).

## 2.9 MIDAS

MIDAS is an atomic force microscope (AFM) coupled with a dust collection and handling system (Riedler et al. 2007; Bentley et al. 2016). Capable of resolutions down to the nanometre level, the AFM operates by scanning a sharp tip over the sample and produces three-dimensional images of collected dust particles. During the outburst event MIDAS was exposing target 13 as part of a 3-day exposure (2016-02-16 23:25:25 until 2016-02-20 05:55:19). Coarse ( $64 \times 64$ ,  $1.25 \mu\text{m}/\text{pixel}$ ) images of the centre of this target immediately showed that new particles had been collected. Since this time a number of scans have been performed to investigate the coverage of this target, in particular to constrain whether the collection represents a large number of individual dust particles or a multitude of fragments originating from a few larger particles impacting the target. These scans are ongoing and the values presented here may change as more data is analysed.

Data have been processed by performing a polynomial plane subtraction and median line correction to remove the scanner-sample slope and correct for distortions during the scan. Particles have then been manually identified and masked. Some areas have no corresponding pre-exposure scans; in these cases it cannot be excluded that the particles are contaminants. However, the morphology of dust on this target is so different from any contaminant detected to date, that the probability of contamination is low. Nonetheless detections smaller than 3 pixels have been excluded here.

The area of the target scanned to date is  $90880 \mu\text{m}^2$  and 135 particles have been identified with an areal coverage of 4.2%. The particle count does not attempt to separate impact fragments from individual particles since the coverage is not yet sufficient to determine this, and thus represents an upper limit. For this reason, a true size distribution of the particles prior to collection cannot yet be established. Instead, some limits are given based on the effective diameters (the diameter of a circle having the same projected area as the particle) of the collected particles or fragments. Ninety percent have an effective size less than  $9.3 \mu\text{m}$  and 50% less than  $3.7 \mu\text{m}$ .

## 2.10 Ground-based observations

Hundreds of ground-based observers, both professional and amateur, have an interest in observing 67P because their data complement the in situ observations by Rosetta. In the following paragraph we present data obtained from a 30 cm amateur telescope and a professional group with a 60 cm telescope. We also report results from a second professional group with a 2 m telescope.

The Rosetta amateur observer campaign (<http://rosetta.jpl.nasa.gov/rosetta-ground-based-campaign>) provides a link between amateur astronomers and the ESA/Rosetta mission. The image provided by Efrain Morales (Fig. 14) shows the coma and tail about 10 days after the outburst. Most of the dust particles seen in the image were emitted after the perihelion passage in summer 2015. However, big mm and cm sized particles from the 2009 perihelion passage also contribute to the brightness in the trail. Particles emitted during the outburst on 19 Feb. 2016 populate the bright central portion of the image.

The robotic 0.6-m telescope TRAPPIST (TRANSiting Planets and Planetesimals Small Telescope; Jehin et al. (2011)) is located at ESO's La Silla Observatory. It is equipped with an FLI ProLine PL3041-BB camera with  $2\text{k} \times 2\text{k}$  pixels of  $15 \mu\text{m}$ . Used with the  $2 \times 2$  binning mode it results in a pixel scale of 1.3 arcsec and a field of view of 22 arcmin. The observations of comet 67P have been performed once or twice a week in 2016 with a Johnson-Cousins Rc filter and with exposure times ranging from 180 to 240 s. TRAPPIST images are reduced following a standard procedure described in Opitom et al. (2015). The sky background is subtracted and the photometric calibration is performed using regular observations of photometric standard stars. The  $Af\rho$  parameter (A'Hearn et al. 1984) is computed at a physical distance from the comet of 5000 km (Fig. 15). The observed brightness has been corrected for the varying phase angle (Sun-67P-observer) using a phase function that is the composite of two different empirical phase functions from Schleicher, Millis, & Birch (1998) and Marcus (2007).

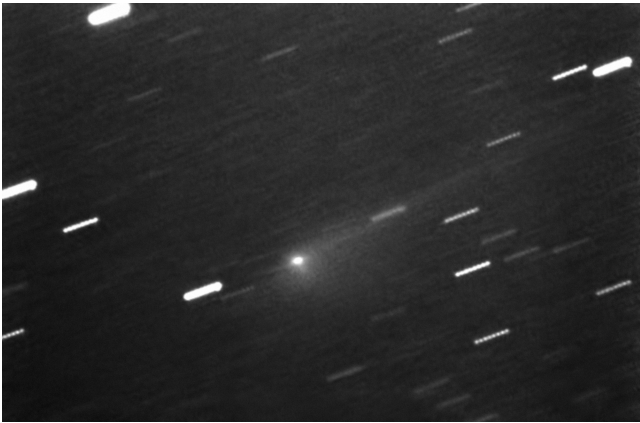


**Figure 14.** Image of 67P taken on 29 Feb. 2016 5:39 UTC taken by Efrain Morales with the 30 cm LX200ACF telescope at Jaicoa Observatory, Puerto Rico, U.S.A.. The CCD image was obtained with a total exposure time of 54 min through a Baader IR filter. The scale of the image is  $2.1 \times 1.4$  million km; the length of the star tracks corresponds to  $\sim 120\,000$  km at the comet's distance.

During the first 100 days of 2016 the phase angle varied from  $28^\circ$  at the beginning of that period, through to a minimum phase angle of  $4^\circ$  at opposition, and finally to  $9^\circ$  at the end of that period. After 19 Feb. 2016 the coma brightnesses in a 5000 km aperture show a clear increase of  $\sim 25\%$  over values from earlier observations. This increased brightness was observed between 29 February and 6 March. The beginning of the brightness increase cannot be precisely determined because of bad weather in the days following the 19 February outburst. On 17 March, the brightness values are back to the normal trend. However, not much of this brightness enhancement remains after the application of the phase function correction because of the opposition surge of the applied empirical phase function, which was derived for observations of 1P/Halley (Schleicher, Millis, & Birch (1998)). The phase correction at low phase angles is rather imperfect and may change after careful comparison with Rosetta observations (see below).

(Boehnhardt et al. 2016) report 67P observations with the 2 m telescope on the Mt. Wendelstein observatory of the University Observatory Munich. Their brightness values after 19 Feb. 2016 deviate clearly beyond measurement uncertainty from the brightness trend using a fit to the earlier observations. However, application of a special phase function reduced the effect of the outburst. Contrary to an earlier outburst of 67P (22-23 August 2015), on 21-22 Feb. 2016 the 67P coma appeared to be undisturbed in terms of geometric dust structures and radial gradient, except for an increase in the brightness.

In Fig. 15 the phase corrected  $Af\rho$  data are compared with the time period (shown by yellow stripes) when all burst particles with speeds  $\geq 4\text{ m s}^{-1}$  are still within the aperture. The observations may show a  $\sim 10\%$  increase of  $Af\rho \sim 10\text{ cm}$  in the burst period compared with the values before the outburst. Later observations display the expected decrease of  $Af\rho$  with heliocentric distance and time.

The long lasting ‘bump’ in the brightness of the comet as seen in the TRAPPIST and in other data sets (Boehnhardt et al. (2016); Snodgrass et al. (2016)) is coincident with the outburst, but also with the comet being at

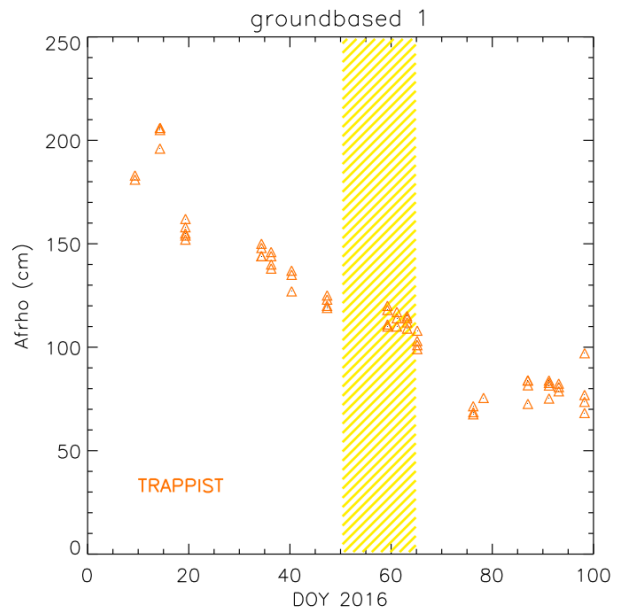


**Figure 15.** Corrected  $Af\rho$  parameters of 67P for the time period from Jan. 9 to April 7, 2016 obtained from observations with the TRAPPIST telescope for apertures of 5000 km. The yellow area marks the times when all burst particles with speeds  $\geq 4\text{ m s}^{-1}$  are within the aperture.

opposition. It may therefore be a combination of a geometric effect and the prolonged increase in activity. There is some indication that the departure from a smooth decrease in  $Af\rho$  starts before 19 February.

To estimate the total dust mass from the increased coma brightness observed with TRAPPIST, we assume that the increase in phase-corrected  $Af\rho$  by approximately 10 cm observed around 19 Feb. 2016 was due to dust released during the outburst on February 19. With  $Af\rho = 4ps^2N/\rho$  (Müller 1999) and assuming a geometric albedo of  $p = 0.05$ , mean particle radius  $s = 100\ \mu\text{m}$ , and aperture radius of  $\rho = 5000\text{ km}$ , we find  $N = 2.5 \times 10^{11}$  particles in the aperture, corresponding to a total dust mass of  $10^3\text{ kg}$  for a bulk density of  $1000\text{ kg m}^{-3}$ .

### 3 DISCUSSIONS

In this section we describe the timing and duration of the outburst that was observed by the different instruments, and we discuss what this can tell us about the properties of the material released by this event. At first we start with the time relation of the data, secondly, we try to identify the time and source region of the outburst, and thirdly, we discuss the magnitude of the outburst. In order to do this we have to make some (not necessarily unanimously agreed) ad hoc assumptions just for the purpose to demonstrate the interrelations between the various observables. Eventually, such assumptions have to come from a comprehensive model of the outburst which is not the task of this first paper.

### 3.1 Time relation of the data

Timing and duration of the outburst can be investigated because the clocks for the different instruments are synchronised with the spacecraft clock. The flight control team makes sure that the spacecraft clock and ground time (UTC) is accurate within less than  $\sim 10$  milliseconds. The measurement of any parameter takes a certain amount of time, which is called the integration time. If the integration time is short ( $< 1$  second), then this is of no concern here. Even if the measurement only takes a short time, the time tagging and the sampling of the available telemetry data points may be much less frequent than that. In the case of the data discussed here we assume that the accuracy of the sampling is of the order of a few seconds. Some images have longer integration times, which can be identified using the image data products, which carry a PDS label keyword `IMAGE_TIME` in the filename that refers to the middle of the integration time. The start and stop time of the integration are given by the `START_TIME` and `STOP_TIME` keywords in the image label files.

All measured parameters discussed above are displayed in Fig. 16 from 9:00 to 13:00 on 19 Feb. 2016. For any given time the ratio of the intensity over the background value at 9:00 is displayed. Most parameters reached their maximum between 10:00 and 11:00. The intensity enhancements during the outburst ranged from  $\sim 20\%$  (RPC-LAP) to a factor of 130 (STR-A). The parameter values at 9:00 and at maximum are also given in Table 1.

The majority of the observations refer to the dust emitted in the outburst (Fig. 17). These dust observations display a significant time lag between the observations by different instruments. The first signature was the dust cloud in the WAC images at 9:40. The next was the significantly enhanced coma brightness ( $\geq 10\%$  of max. value above background) observed by Alice at 9:51 followed at 9:58 by STR-A. Maximum brightness was observed by the OSIRIS WAC and NAC at 10:10. The GIADA smoothed count rate exceeded 10% of maximum value above background at 10:42, and the trailed NAC images of near-by individual grains were observed at and after 11:40.

The enhanced coma brightness observed by Alice and OSIRIS refer to dust near the nucleus and their order is mostly determined by the respective sequence of observations. In contrast, the enhanced signatures in the STR-A, GIADA, and OSIRIS near-by grain data represent a clear time-of-flight relation of grains of different sizes and emission speeds. The mean speed of the GIADA grains (GDS\_IS) is  $6.5 \text{ m s}^{-1}$  and the mean mass is  $4 \times 10^{-8} \text{ kg}$ , which corresponds to a radius of about  $180 \mu\text{m}$  (at an assumed density of  $1000 \text{ kg m}^{-3}$ ).

For the STR-A camera to see any dust from the outburst, the emitted grains had to have traversed the distance of  $\sim 30 \text{ km}$  from the nucleus to the STR-A FOV. Therefore, the fastest particles that were seen by STR-A had to have a speed of at least  $25 \text{ m s}^{-1}$ . The majority of them had speeds between 5 and  $10 \text{ m s}^{-1}$ . Similarly, the particles that had trails in the OSIRIS images had speeds of  $\leq 4 \text{ m s}^{-1}$ .

If we assume a speed-radius dependence of  $v \sim s^{-0.5}$  then the particle sizes range from  $\sim 10 \mu\text{m}$  for the fastest STR-A particles to  $\sim 300 \mu\text{m}$  for the OSIRIS individual par-

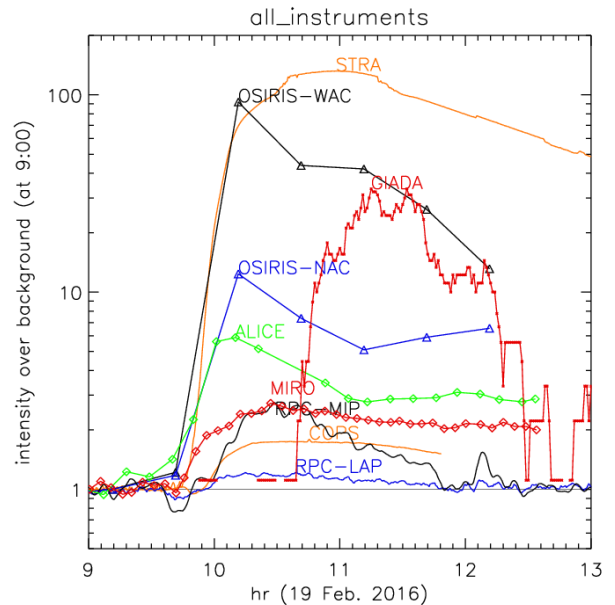


**Figure 16.** Intensity ratio of the measured parameters over the intensity measured at 9:00.

ticles. The smallest particles ( $\leq 10 \mu\text{m}$ ) were those collected by MIDAS.

The earliest indication of gas in the outburst was observed by MIRO at 9:52 (Fig. 18). This is within a minute of the earliest dust observations by Alice. Both LOSs are very close to each other. However, Alice measurements refer to dust near the nucleus while the MIRO signal is assumed to originate near Rosetta.

ROSINA COPS detected significant gas density increase ( $> 10\%$  of maximum) at the position of Rosetta at 9:57. There was a small dip in the gas density ( $\sim 10\%$  of the following enhancement) for  $\sim 10$  minutes just prior to the strong rise of the signal.

RPC-MIP observed an increase of the electron density at Rosetta at 10:00. However, a significant reduction of the electron density started already at 9:38, just at the expected time of the outburst. The dip in the electron density had an amplitude of  $\sim 15\%$  of the following enhancement.

The spacecraft potential monitored by RPC-LAP followed closely the course of the electron density becoming more negative at higher electron densities. At 9:00 the mean S/C potential was about  $-16.7 \text{ V}$ ; by 9:42 it was  $-15 \text{ V}$  and became rapidly more negative reaching  $-20 \text{ V}$  around 10:20. During the following 3 hours the S/C potential excursion decreased to the normal value of  $\sim -16 \text{ V}$ .

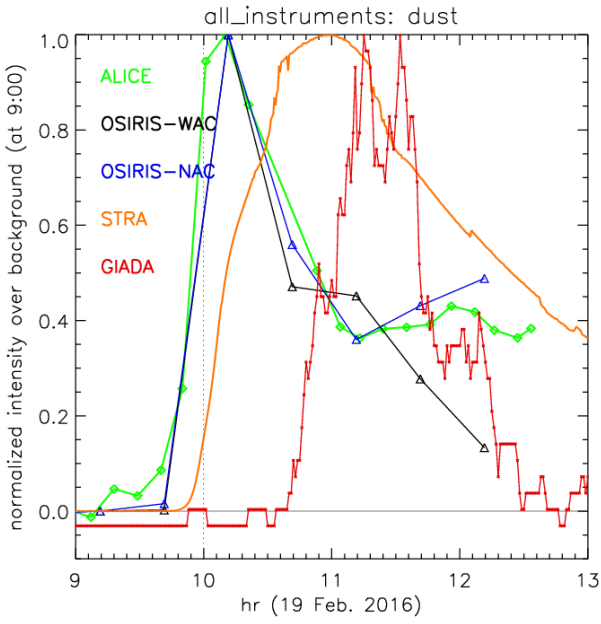
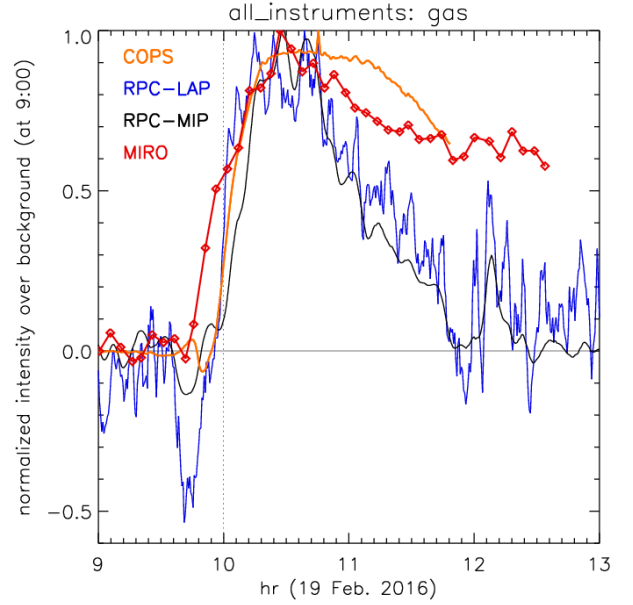
### 3.2 Time and source region of the outburst

The first sign of outburst was seen at 9:40 in the OSIRIS image (Fig. 3) close to the shadow region. Fig. 19 shows the same image with isophotes. The bottom centre brightness originates from the dust cloud that was generated in the outburst and became illuminated by the Sun. Figure 2 shows the model scene with the complete nucleus and the shadow at 9:40 but without the dust cloud.

The potential source region is in the centre at or be-

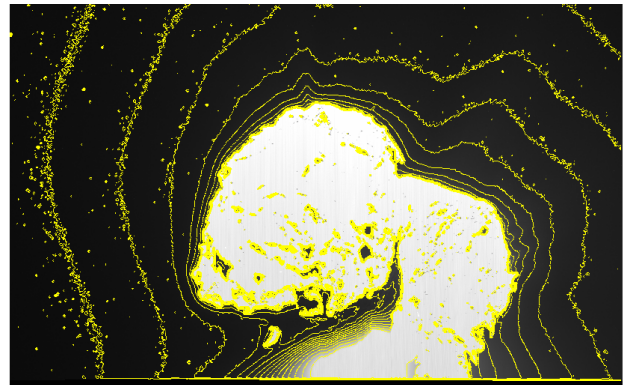
**Table 1.** Measurement parameters at 9:00 and at maximum.

Instrument	Parameter	Value at 9:00	Maximum value	Factor	Time at maximum
OSIRIS WAC	Surface brightness [ $\text{W m}^{-2} \text{sr}^{-1} \text{nm}^{-1}$ ]	$5.1 \times 10^{-7}$	$4.7 \times 10^{-5}$	91.9	10 : 11.5
OSIRIS NAC	Surface brightness [ $\text{W m}^{-2} \text{sr}^{-1} \text{nm}^{-1}$ ]	$1.75 \times 10^{-6}$	$2.17 \times 10^{-5}$	12.3	10 : 11.5
Alice	Surface brightness [rayleighs]	84.0	494.1	5.88	10 : 10.1
MIRO	Antenna temperature in the $\text{H}_2^{16}\text{O}$ line [K]	19.4	53.0	2.73	10 : 26.9
RPC LAP	Spacecraft potential [V]	-16.7	-20.3	1.22	10 : 38.6
RPC MIP	Electron density [ $\text{cm}^{-3}$ ]	$\sim 440$	$\sim 1200$	2.7	10 : 37.6
ROSINA COPS	Gas density [ $\text{cm}^{-3}$ ]	$0.83 \times 10^8$	$1.49 \times 10^8$	1.80	10 : 45.3
STR-A	Brightness [ $\text{W m}^{-2} \text{sr}^{-1} \text{nm}^{-1}$ ]	$2.6 \times 10^{-8}$	$3.43 \times 10^{-6}$	132.1	10 : 58.2
GIADA	Dust count rate [ $\text{min}^{-1}$ ]	0.1	3.33	33.3	11 : 15.0


**Figure 17.** Normalized intensity (to maximum) of dust observations

**Figure 18.** Normalized intensity (to maximum) of gas and plasma observations

low the edge of the WAC image (in region Seth, Anubis, or Atum). The brightness of the dust cloud is in saturation. Most of the scene below the WAC image is in the shadow except for a cliff that just appeared in full sunlight. The gradient of the isophotes in the lower part of the image (Fig. 19) points to a maximum brightness close to the illuminated cliff which is  $\sim 700$  m below the edge of the image. At an expansion speed of  $\sim 25 \text{ m s}^{-1}$  the time for the cloud to enter the FOV of the WAC camera is  $\lesssim 120$  s. This brings the outburst time to  $9:38 \pm 1$  minute. The centre coordinates of the illuminated cliff are in the Atum region at longitude  $232.3^\circ$ , latitude  $-28.6^\circ$ , and radius 1738 m.

The outburst started close to the morning terminator and the source region rotated at a rate of  $\sim 30^\circ/\text{hour}$  into the Sun direction; at about 13:00 on 19 Feb. the source region was near the subsolar limb and at about 16:00 the source region reached the evening terminator and entered comet night.


**Figure 19.** OSIRIS WAC image at 9:40 with isophotes. The isophotes are separated by a factor 1.4 with the innermost isophote at a brightness of  $10.54 \times 10^{-5} \text{ W m}^{-2} \text{sr}^{-1} \text{nm}^{-1}$  (just below the saturation limit).

### 3.3 Magnitude of the outburst

The peak brightnesses observed by Alice and OSIRIS provide a means to estimate the magnitude of the outburst. The increase in mean coma brightness in the 175–195 nm bandpass is  $\sim 370$  rayleighs. This translates to a radiance of  $I = 1.58 \times 10^{-8} \text{ W m}^{-2} \text{ nm}^{-1} \text{ sr}^{-1}$  at 185.5 nm. The solar radiance at 185.5 nm and at 2.4 AU is  $1.58 \times 10^{-4} \text{ W m}^{-2} \text{ nm}^{-1} \text{ sr}^{-1}$  so  $I/F = 1.0 \times 10^{-4}$ . From OSIRIS NAC we find  $I/F \sim 3 \times 10^{-5}$  before the outburst and  $\sim 2 \times 10^{-4}$  after the outburst, in good agreement with the Alice result. The filling factor, or optical depth,  $\tau$ , is given by  $I/F = pj(\alpha)\tau$ , where  $p$  is the geometric albedo and  $j(\alpha)$  is the phase function. Assuming that the dust has the same properties as the nucleus (Feaga et al. 2015),  $p = 0.04$ ,  $j(63^\circ) = 0.10$ , so  $\tau = 0.025$ . OSIRIS WAC finds  $\tau = 0.01$  before and  $\tau = 0.1$  immediately after the outburst. This difference is not surprising since the LOSs of both instruments are different in relation to the centre of the outburst. Future detailed analysis and modelling the scattering properties of dust of different sizes at different wavelengths along similar LOSs may provide information on the size distribution of the particles. In addition the total cross-section of particles generated in the outburst may be estimated by modelling the particles' emission.

There is another way to calculate the total cross-section of the emitted particles; this is from the in situ measurements by GIADA and MIDAS. MIDAS found an areal coverage of 4.2% of bigger than  $1 \mu\text{m}$ -radius particles. The total area of the GIADA IS detector is  $10^{-2} \text{ m}^2$ . The total cross-section of all particles detected during outburst by GIADA is  $7 \times 10^{-6} \text{ m}^2$  corresponding to  $1.2 \times 10^{-3}$  coverage of  $> 100 \mu\text{m}$ -radius particles. Scaling the dust coverage to 2 km i.e.  $\sim 1/20$ th of the Rosetta distance then an optical depth of 1 is reached. This value is compatible with the saturated brightness of the inner dust cloud in the OSIRIS WAC image at 9:40. If detailed analysis confirms these values then during the outburst the dominant cross-section is in the MIDAS particles of radius  $< 100 \mu\text{m}$ .

The total mass of  $> 100 \mu\text{m}$ -radius particles detected by the  $10^{-2} \text{ m}^2$  GIADA IS and GDS sensors at 35 km from the nucleus is  $1.33 \times 10^{-6} \text{ kg}$ . If we assume that a similar mass flux of dust particles was emitted into a solid angle  $\Omega_d = 1 \text{ sr}$  then the total mass  $M_{100\mu\text{m}} = 1.6 \times 10^3 \text{ kg}$  not counting any mass contribution by smaller and much bigger particles. This mass is about 1.6 times the mass derived from  $Af\rho$  measurements in ground-based observations (Section 2.10). The width of the emission was therefore probably narrower than assumed above. The interpretation of the ground-based observations may also be improved by the comparison with Rosetta observations.

Similarly, the gas production can be estimated from the measured extra gas density  $n_g \sim 5 \times 10^7 \text{ cm}^{-3}$  at Rosetta. We assume that the gas from the outburst is emitted into a solid angle  $\Omega_g = 2\pi \text{ sr}$  with a speed  $v_g \sim 600 \text{ m s}^{-1}$ . The gas production rate in the outburst is then  $Q_g = \Omega_g r_{ROS}^2 v_g n_g \approx 2.3 \times 10^{26} \text{ s}^{-1}$  corresponding to  $\sim 10 \text{ kg s}^{-1}$   $\text{H}_2\text{O}$ ,  $\text{CO}_2$ , and  $\text{CO}$ . The duration of the enhanced gas density was about 2 hours; therefore a total of  $\sim 7 \times 10^4 \text{ kg}$  of gas was emitted during the outburst. This exceeds the total amount of dust detected by GIADA by at least a factor of 40, giving a lower limit for the dust-to-gas-mass-ratio of  $\sim 0.025$ . During the

background emission Fulle et al. (2016) estimate the dust-to-gas-mass-ratio to be  $\sim 6$  or larger.

## 4 CONCLUSIONS

The outburst on 19 Feb. 2016 was unexpected, but serendipitously most Rosetta instruments were in suitable measuring conditions while the outburst unfolded. This was very special because for the many outbursts during perihelion passage (July to September 2015, Vincent et al. (2016)) we never had the situation that that many instruments observed the same outburst at once. In particular, the in-situ dust instruments did not make significant observations of these outbursts. This was due to the large distances (up to 400 km) Rosetta had to maintain for safety reasons. The unique circumstances of the 19 February outburst enabled the in-situ instruments to provide important measurements to quantify the outburst.

The likely outburst location in the Atum region at latitude  $-28.6^\circ$  and longitude  $+232.3^\circ$  (Fig. 20) is interesting because two other outbursts observed in 2015 were in the immediate vicinity Vincent et al. (2016). They were outburst #15 observed by NAVCAM on 2015-08-01T15:44 at latitude  $-32^\circ$ , longitude  $= +227^\circ$  and #23 observed by OSIRIS-NAC on 2015-08-28T13:36 at latitude  $= -31^\circ$ , longitude  $= +229^\circ$ .

The location of these outbursts is on the eastern slope of the body of 67P. It is in a region of a steep cliff to the east. The fact that the outburst started when this region just exited the shadow from the head suggests that thermal stress in the surface material may have triggered a landslide that exposed fresh (water) ice to direct solar illumination. Also other features of the observations support that idea: (1) the relative long duration of the GIADA dust impact phase which tells that the dust cone is very broad, (2) from looking at OSIRIS pictures, where one sees a cloud, not a narrow jet (3) from the fact that it is probably driven by water only. In this scenario the trigger of activity is thermal stress together with fracture mechanics and gravity in form of landslides or avalanches before solar heat can release gas from fresh ice which in turn accelerates dust released during this process.

At present, it is difficult to infer the nature of the icy material exposed to solar illumination. Recent simulations show that, in addition to sublimation of crystalline ice, clathrate destabilization and amorphous ice crystallization can lead to the formation of outbursts and pits with shapes consistent with those observed in the Seth region (Mousis et al. 2015). A proof of these ideas would come from the composition of the gas during this outburst. If the gas is lacking highly volatile species such as  $\text{CO}$ ,  $\text{N}_2$  or  $\text{Ar}$ , it would mean that the sublimating icy layer is close to the surface and was already partly devolatilized before, as shown by thermal evolution models (Mousis et al. 2015). Part of it could even be reprocessed water ice. In this case the outburst was not the 'jet' revealing fresh material from the interior, but just a surface effect. It may look completely different from the gas composition perspective than the outbursts last summer, where all volatiles except water peaked.

A further interesting feature of this outburst is that the gas production decreased much faster than expected from

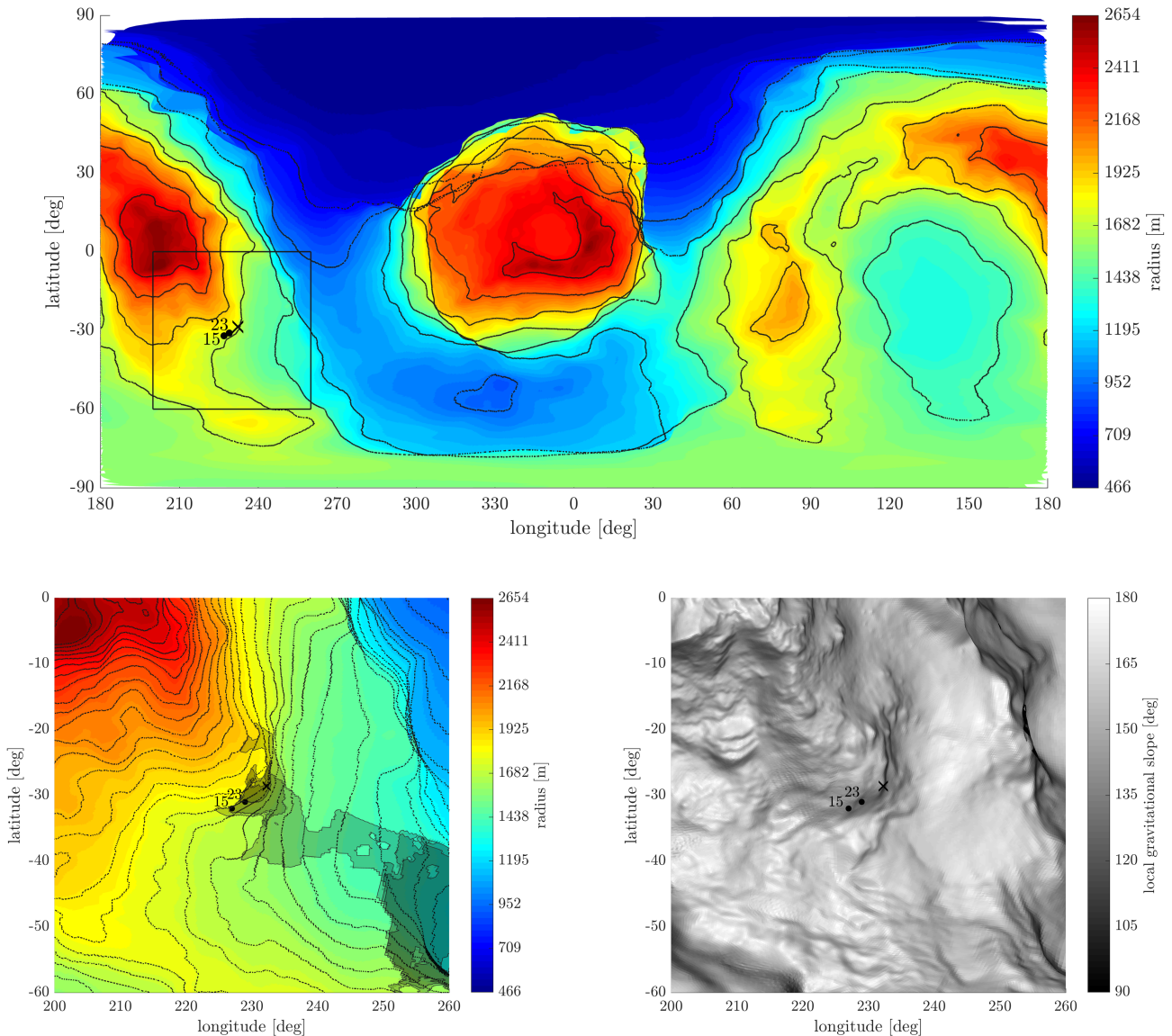


**Figure 20.** Terrain maps of 67P. Outburst positions are marked by X (19 Feb. 2016 outburst) and by numbers (cf. Vincent et al. (2016)). Top: radius map showing the elevated head region in the centre and the body at the left (West) and right (East) fringes. Lower left: enlarged radius map showing the outburst position (x). The contour lines are separated by 50 m. Gray shading represent illuminated areas at 9:40 (dark gray), 9:50 (middle gray), and 10:00 (light gray). Lower right: topographic map in which the gray shading represents the local slope, accounting for gravity and centrifugal force (white=flat, black=vertical wall).

direct solar illumination. This may suggest that building up of a dust mantle quenched the gas emission. This outburst will trigger many further studies in the near future.

## ACKNOWLEDGEMENTS

Rosetta is an ESA mission with contributions from its member states and NASA. Rosetta’s Philae lander is provided by a consortium led by DLR, MPS, CNES and ASI. We thank all elements of the Rosetta project for the magnificent job they are doing to make this mission an astounding success. The Alice team acknowledges

continuing support from NASA’s Jet Propulsion Laboratory through contract 1336850. GIADA/Univ Parthenope NA/INAF/OAC/IAA/INAF-IAPS: this research was supported by the Italian Space Agency (ASI) within the ASI-INAF agreements I/032/05/0 and I/024/12/0. OSIRIS was built by a consortium of the Max-Planck- Institut für Sonnensystemforschung, Göttingen, Germany, CISAS University of Padova, Italy, the Laboratoire d’Astrophysique de Marseille, France, the Instituto de Astrofísica de Andalucía, CSIC, Granada, Spain, the Research and Scientific Support Department of the European Space Agency, Noordwijk, The Netherlands, the Instituto Nacional de Técnica Aeroespacial, Madrid, Spain, the Universidad Politécnica

de Madrid, Spain, the Department of Physics and Astronomy of Uppsala University, Sweden, the UK(STFC), and the Institut für Datentechnik und Kommunikationsnetze der Technischen Universität Braunschweig, Germany. The support of the national funding agencies of Germany (DLR), France(CNES), Italy(ASI), Spain(MEC), Sweden(SNSB), and the ESA Technical Directorate is gratefully acknowledged. Work at LPC2E/CNRS was supported by CNES and by ANR under the financial agreement ANR-15-CE31-0009-01. Work on ROSINA COPS at the University of Bern was funded by the State of Bern, the Swiss National Science Foundation and by the European Space Agency PRODEX program. O.M.: this work has been partly carried out thanks to the support of the A\*MIDEX project (n° ANR-11-IDEX-0001-02) funded by the “Investissements d’Avenir” French Government program, managed by the French National Research Agency (ANR). This work also benefited from the support of CNRS-INSU national program for planetology (PNP).

## REFERENCES

- A’Hearn M. F., Schleicher D. G., Millis R. L., Feldman P. D., Thompson D. T., 1984, *AJ*, 89, 579  
 Balsiger H., et al., 2007, *SSRv*, 128, 745  
 Bentley M. S., et al., 2016, *Acta Astronautica*, in press  
 Bieler A., et al., 2015, *A&A*, 583, A7  
 Boehnhardt H. et al., 2016, *MNRAS*, this issue  
 Buemi M., Landi A., Procopio D., 2000, *ESASP*, 425, 279  
 Burch J. L., Goldstein R., Cravens T. E., Gibson W. C., Lundin R. N., Pollock C. J., Winningham J. D., Young D. T., 2007, *SSRv*, 128, 697  
 Carr C., et al., 2007, *SSRv*, 128, 629  
 Colangeli L., et al., 2007, *SSRv*, 128, 803  
 Della Corte V. et al., 2014, *J. Astron. Instrum.*, 03, 1350011  
 Della Corte V. et al., 2015, *A&A*, 583, A13  
 Della Corte V. et al., 2016, *Acta Astronautica*, 126, 205  
 Della Corte V. et al., 2016, *MNRAS*, this issue  
 Eriksson A. I., et al., 2007, *SSRv*, 128, 729  
 Feaga L. M., et al., 2015, *A&A*, 583, A27  
 Feldman P. D., et al., 2015, *A&A*, 583, A8  
 Ferrari M., Della Corte V., Rotundi A., Rietmeijer F.J.M., 2014, *Planet. Space Sci.*, 101, 53  
 Fulle M. et al., 2015, *ApJ Lett.*, 802, L12  
 Fulle M. et al., 2016, *MNRAS*, this issue  
 Glassmeier K.-H., et al., 2007, *SSRv*, 128, 649  
 Glassmeier K.-H., Boehnhardt H., Koschny D., Kührt E., Richter I., 2007, *SSRv*, 128, 1  
 Gulkis S., et al., 2007, *SSRv*, 128, 561  
 Geiger B. et al., in prep  
 Geiger and Barthelemy, 2016, *ROSETTA ORBITER NAVCAM EXT1-MTP026, RO-C-NAVCAM-2-EXT1-MTP026-V1.0*  
 Hässig M., et al., 2015, *Sci*, 347, aaa0276  
 Hofstadter M. et al., in prep  
 Jehin E., et al., 2011, *Msngr*, 145, 2  
 Keller H. U., et al., 2007, *SSRv*, 128, 433  
 Marcus J. N., 2007, *ICQ*, 29, 39  
 Mousis O., et al., 2015, *ApJ*, 814, L5  
 Müller M., 1998, *ESOC Report RO-ESC-TA-5501*  
 Opitom C., Jehin E., Manfroid J., Hutsemékers D., Gillon M., Magain P., 2015, *A&A*, 584, A121  
 Rotundi A. et al., 2015, *Science*, 347, aaa3905  
 Riedler W., et al., 2007, *SSRv*, 128, 869  
 Schleicher D. G., Millis R. L., Birch P. V., 1998, *Icar*, 132, 397  
 Sierks H., et al., 2015, *Sci*, 347, aaa1044  
 Snodgrass C. et al., in prep  
 Stern S. A., et al., 2007, *SSRv*, 128, 507  
 Stern S. A., et al., 2015, *Icar*, 256, 117  
 Trotignon J. G., et al., 2007, *SSRv*, 128, 713  
 Vincent J.-B. et al., 2016, *MNRAS*, this issue  
 Vincent J.-B., et al., 2016, *A&A*, 587, A14

This paper has been typeset from a  $\text{\TeX}/\text{\LaTeX}$  file prepared by the author.